Fluid Dynamics &
Materials Processing

Tech Science Press

http://doi.org/10.32604/fdmp.2026.082597

ARTICLE

Laminar Forced Convection over a Non-Isothermal Wedge in a Hybrid Nanofluid with Internal Heat Generation, Thermal Radiation, and Surface Transpiration Effects

Ken-Ming Tu*

Department of Aircraft Engineering, Air Force Institute of Technology, Kaohsiung City, Taiwan
*Corresponding Author: Ken-Ming Tu. Email: dg9592@gmail.com

Received: 22 March 2026; Accepted: 18 May 2026; Published: 30 June 2026

ABSTRACT: This study presents a comprehensive numerical investigation of laminar forced convective boundary layer flow over a non-isothermal wedge immersed in an Al_2O_3-Cu/water hybrid nanofluid, with relevance to thermal management in high-temperature aerospace systems, microelectronic cooling devices, and nuclear safety components. The research evaluates the combined effects of exponential space-dependent heat generation (ESDHG), thermal radiation, and uniform surface transpiration (suction/blowing) on the hydrothermal performance of the system. The governing non-similar differential equations, incorporating the Rosseland diffusion approximation, are solved using the high-accuracy Keller-box method. The numerical results indicate that increasing the wedge angle parameter compresses the momentum boundary layer, consequently enhancing both the local skin-friction coefficient and the Nusselt number. A key finding is the emergence of a temperature overshoot phenomenon under strong internal heat generation, leading to local heat flux reversal from the fluid toward the solid boundary. This behavior identifies a critical limitation in thermal regulation, showing that excessive internal heating can degrade the cooling effectiveness of the hybrid nanofluid.

KEYWORDS: Hybrid nanofluid; thermal management; temperature overshoot; forced convection; non-isothermal wedge; exponential heat generation

1 Introduction

Investigating boundary layer characteristics over various geometric shapes is a fundamental area in fluid dynamics, grounded in the classical frameworks established by Schlichting and Gersten [1]. Early approximate solutions for boundary layer equations concerning wedge flows were formulated by Falkneb and Skan [2]. Subsequent research broadened these concepts to include intricate thermal conditions and porous surfaces. For instance, Koh and Hartnett [3] explored heat transfer and skin friction within laminar flows moving across porous wedges subjected to variable wall temperatures and suction. Ye-Mon [4], along with Lin and Lin [5], further refined the comprehension of heat transfer mechanisms across diverse Prandtl numbers using similarity solutions. Implementing flow control via permeable surfaces is crucial for modern thermal management applications. Watanabe [6] and Yih [7] performed detailed analyses on how uniform blowing or suction impacts forced convection over isothermal surfaces and wedges experiencing uniform heat flux. In recent years, investigations into boundary layer flows have progressively incorporated a variety of complex physical mechanisms to better reflect real-world engineering conditions. Extensive research has been conducted on mixed convection within

highly porous materials, temperature-dependent viscosity, and magnetohydrodynamic (MHD) effects over moving wedges or rotating bodies [8–12]. Within high-temperature engineering contexts, such as nuclear reactor safety and waste management, internal heat generation remains a critical factor. Hussain et al. [13] pioneered exponential decay models for space-dependent heat generation, a framework further expanded by Postelnicu et al. [14] to account for variable viscosity in porous media. Concurrently, thermal radiation often becomes the dominant energy transport mechanism under significant temperature gradients; thus, many studies have successfully utilized the Rosseland diffusion approximation to simulate these radiative impacts across complex geometries [15–19]. Building on these foundations, recent literature has specifically evaluated the performance of thermal radiation in hybrid nanofluids over wedge geometries and porous media [20–22]. Furthermore, the coupled interplay between complex internal heating and surface transpiration (suction/blowing) effects has been explored to further understand fluid heat transport variations [23–25]. These established studies on MHD, exponential space-dependent heat generation (ESDHG), Rosseland radiation, and transpiration provide a comprehensive theoretical framework for the current investigation into hybrid nanofluid hydrothermal behavior over a non-isothermal wedge.

To overcome the thermal limitations of standard coolants, Choi [26] introduced the concept of "nanofluids"—base liquids infused with nanoparticles to boost thermal conductivity. Contemporary research has progressively focused on hybrid nanofluids, which blend multiple types of nanoparticles to achieve enhanced thermal performance in various engineering applications [27–30]. Recent investigations have analyzed the hydrothermal properties of nanofluids flowing over wedges under diverse conditions, including convective boundary constraints and MHD effects [31–35]. The theoretical frameworks developed by Tiwari and Das [36], as well as Oztop and Abu-Nada [37], provide the foundation for assessing the thermophysical characteristics of these advanced mixtures.

Although extensive literature exists regarding Falkner-Skan flows and hybrid nanofluids, the precise interactions among exponential space-dependent heat generation (ESDHG), thermal radiation, and uniform blowing/suction within a water-based hybrid nanofluid system remain inadequately explored. This research addresses this literature gap by utilizing the Keller box method to computationally model these coupled effects, thereby yielding critical insights for designing cooling surfaces in high-temperature industrial processes [38–41]. Additional computational methodologies have also been explored to optimize thermal systems [42–44]. The specific selection of an Al_2O_3-Cu/water hybrid nanofluid is strategic: Al_2O_3 provides excellent chemical stability and oxidation resistance, while Cu contributes exceptionally high thermal conductivity, overcoming the limitations of single-particle nanofluids.

Current investigations into hybrid nanofluids frequently emphasize multifaceted thermal enhancements across diverse engineering configurations. For example, Alwan et al. [45] recently conducted a comprehensive analysis of internal convection within triangular cavities, incorporating porous wavy fins alongside magnetohydrodynamic and radiative effects. While such enclosure-centric models deliver valuable insights into constrained fluid dynamics, their findings do not directly translate to the behavior of unconfined systems. Consequently, the present research shifts the focus from internal convective mechanisms to the distinct hydrodynamic characteristics of external boundary layer flows.

To bridge the existing knowledge gap regarding external aerodynamic surfaces, this study examines forced convection past a non-isothermal wedge. The primary novelty lies in coupling this flow with exponential space-dependent heat generation (ESDHG) and uniform surface transpiration (blowing/suction). By utilizing a non-similar formulation, the current model accurately tracks the fluid's spatial progression along the wedge—a continuous streamwise evolution inherently restricted in confined enclosure studies. This specific setup facilitates a rigorous characterization of critical thermal management parameters, particularly the

"temperature overshoot" effect and subsequent heat-flux reversal. Although basic Falkner-Skan flows have been extensively documented, the complex interplay among thermal radiation, ESDHG, and surface mass flux within a water-based hybrid nanofluid remains insufficiently explored. By employing the Keller-box algorithm to resolve these multiphysics interactions, this work not only fills a critical literature void but also provides robust theoretical guidelines for optimizing cooling surfaces in high-temperature industrial applications.

Despite advances in confined cavity flows, the coupled effects of spatial heat generation, thermal radiation, and transpiration on the external boundary-layer evolution of hybrid nanofluids remain unresolved. This study addresses this gap by formulating a continuous streamwise non-similar model over a permeable wedge to determine the precise thermodynamic thresholds where standard convective cooling fails.

2 Mathematical Models

The present theoretical framework considers a steady, two-dimensional, laminar forced convective boundary layer flow traversing a permeable wedge. The wedge is characterized by a half-angle γ and is submerged within a continuously flowing water-based hybrid nanofluid. This model systematically incorporates the coupled phenomena of thermal radiation and exponential space-dependent internal heat generation. As geometrically outlined in Fig. 1, the Cartesian coordinate system originates at the wedge's leading edge (denoted as point o). Here, the x-axis aligns with the wedge surface, while the y-axis is orthogonal to it. The fluid is subjected to a uniform surface mass flux V_w (blowing or suction), and the wedge surface is maintained at a variable temperature $T_w(x)$ that constantly exceeds the free-stream ambient temperature T_∞.

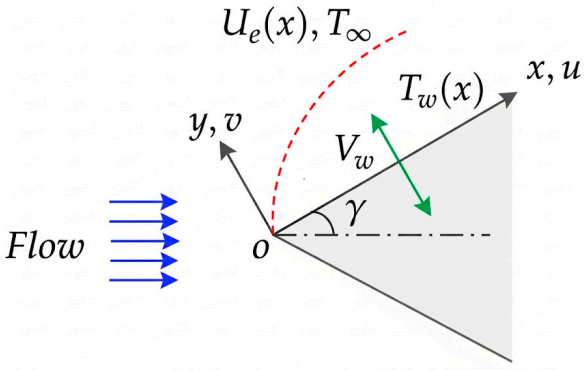

Figure 1: The physical configuration and spatial coordinates of the fluid flow model.

The formulation is predicated on several fundamental assumptions: the flow is steady, two-dimensional, incompressible, and laminar. Viscous dissipation is deemed negligible, and the Al_2O_3-Cu/water hybrid nanofluid is treated as a continuous, single-phase homogeneous mixture in thermal equilibrium. Additionally, by assuming an incompressible flow, the model fundamentally neglects fluid compressibility and property variations (other than viscosity) under extreme high-temperature gradients, which could play a secondary role in high-speed aerodynamic heating.

Based on standard boundary layer approximations and omitting viscous dissipation effects, the fundamental conservation laws for mass, momentum, and energy are formulated. The radiative heat flux is modeled utilizing the Rosseland diffusion approximation [19,42], while the thermophysical behaviors

of the hybrid nanofluid adopt the correlations validated by Murad et al. [41]. Guided by the classical formulations of Watanabe [6], the governing partial differential equations are established as:

Conservation of mass:

$$\frac{\partial u}{\partial x}+\frac{\partial v}{\partial y}=0 \tag{1}$$

Conservation of momentum: boundary layer

$$u\frac{\partial u}{\partial x}+v\frac{\partial u}{\partial y}=U_e(x)\frac{dU_e(x)}{dx}+\frac{\mu_{hnf}}{\rho_{hnf}}\frac{\partial^2 u}{\partial y^2} \tag{2}$$

Conservation of energy:

$$\begin{aligned} &u\frac{\partial T}{\partial x}+v\frac{\partial T}{\partial y}\\ &=\frac{k_{hnf}}{(\rho C_P)_{hnf}}\frac{\partial^2 T}{\partial y^2}-\frac{1}{(\rho C_P)_{hnf}}\frac{\partial q_{rad}}{\partial y}+\frac{q'''}{(\rho C_P)_{hnf}} \end{aligned} \tag{3}$$

Rosseland diffusion approximation:

$$q_{rad}=-\frac{4\sigma_o}{3\chi}\frac{\partial T^4}{\partial y} \tag{4}$$

The corresponding boundary constraints are prescribed as:

$$y=0\ :\ u=0, v=V_w, T=T_w\big(x\big)=T_\infty+Ax^\lambda, \tag{5}$$

$$y\to\infty\ :\ u=U_e(x), T=T_\infty. \tag{6}$$

$$U_e(x)=Bx^m, m=\gamma/(\pi-\gamma) \tag{7}$$

within these expressions, u and v represent the velocity components along the x and y-axes, whereas T denotes the fluid temperature. The constant A is strictly positive, and λ functions as the variable wall temperature (VWT) power-law exponent; notably, $\lambda=0$ simplifies the model to a uniform wall temperature (UWT). The velocity of the external free stream is defined by $U_e(x)=Bx^m$, where B acts as a structural constant and $m=\gamma/(\pi-\gamma)$ designates the wedge angle parameter. Geometrically, $m=0$, $m=1/3$, and $m=1$ simulate flows over a flat plate, a right-angled (90°) wedge, and an orthogonal stagnation surface, respectively.

Regarding the thermal radiation modeled via Eq. (4), q_{rad} identifies the radiative heat flux, σ_0 is the Stefan-Boltzmann constant, and χ signifies the Rosseland mean absorption coefficient. By presuming minimal temperature gradients within the flow domain, the term T^4 is linearized utilizing a Taylor series expansion centered on the free-stream temperature T_∞. Truncating higher-order components yields (Eq. (8)). The adoption of the Rosseland diffusion approximation is strictly predicated on the condition that the working fluid behaves as an optically thick medium. This implies that the fluid-nanoparticle mixture possesses intense absorption and scattering capabilities, rendering the radiation mean free path substantially smaller than the characteristic length of the thermal boundary layer. While this approximation is robust for many macroscopic analyses, its application to extreme high-temperature environments necessitates

caution; if the medium becomes optically thin under specific conditions, this localized diffusion model may underestimate the long-range transport effects of radiative heat transfer.

$$T^4 \cong 4T_\infty^3 T - 3T_\infty^4 \tag{8}$$

To accurately capture the mixture's physical characteristics, the effective dynamic viscosity (μ_{hnf}) of the hybrid nanofluid is correlated with the base fluid viscosity (μ_f) through the volume fractions of the alumina (φ_1) and copper (φ_2) nanoparticles, expressed as:

$$\frac{\mu_{hnf}}{\mu_f} = \frac{1}{(1-\varphi_1)^{2.5}(1-\varphi_2)^{2.5}} \tag{9}$$

When both volume fractions are zero ($\varphi_1 = \varphi_2 = 0$), the model naturally reverts to a standard Newtonian base fluid. Furthermore, the mixture's effective density (ρ_{hnf}), thermal conductivity (k_{knf}), and volumetric heat capacity ($(\rho C_P)_{hnf}$) are synthesized from the individual properties of the base liquid and suspended solid particles according to the following phenomenological relations:

$$\frac{\rho_{hnf}}{\rho_f} = (1-\varphi_2)\left(1-\varphi_1+\varphi_1\frac{\rho_{n1}}{\rho_f}\right)+\varphi_2\frac{\rho_{n2}}{\rho_f} \tag{10}$$

$$\frac{k_{knf}}{k_{nf}} = \frac{k_{n2}+2k_{nf}-2\varphi_2\left(k_{nf}-k_{n2}\right)}{k_{n2}+2k_{nf}+\varphi_2\left(k_{nf}-k_{n2}\right)}, \frac{k_{nf}}{k_f} = \frac{k_{n1}+2k_f-2\varphi_1\left(k_f-k_{n1}\right)}{k_{n1}+2k_f+\varphi_1\left(k_f-k_{n1}\right)} \tag{11}$$

$$\frac{\left(\rho C_p\right)_{hnf}}{\left(\rho C_p\right)_f} = (1-\varphi_2)\left[1-\varphi_1+\varphi_1\frac{\left(\rho C_p\right)_{n1}}{\left(\rho C_p\right)_f}\right]+\varphi_2\frac{\left(\rho C_p\right)_{n2}}{\left(\rho C_p\right)_f} \tag{12}$$

The specific baseline thermophysical properties for the pure water and respective nanoparticles are systematically cataloged in Table 1.

While the present mathematical framework treats the Al_2O_3-Cu/water hybrid nanofluid as a homogeneous, single-phase continuum characterized by effective thermophysical properties, it is essential to acknowledge the inherent limitations of this classical approach. This macroscopic formulation fundamentally neglects micro-scale solid-fluid interactions, such as Brownian motion and thermophoretic forces, which can induce relative slip velocities between the suspended nanoparticles and the base fluid. Furthermore, in practical high-temperature engineering applications, the potential for nanoparticle agglomeration or sedimentation could locally alter the mixture's effective thermal conductivity and flow dynamics, thereby causing deviations from the idealized homogeneous mixture assumption.

Table 1: Thermophysical parameters of the base fluid and nanoparticles utilized in the study by Ahmad et al. [38].

Physical Properties	Fluid Phase (Water)	Al_2O_3	Cu
C_P (J/kg K)	4179	765	385
ρ (kg/m^3)	997.1	3970	8933
k (W/m K)	0.613	40	400

A stream function $\psi(x, y)$ is introduced, defining $u = \partial\psi/\partial y$ and $v = -\partial\psi/\partial x$, which intrinsically satisfies the mass conservation principle. The mathematical domain is subsequently mapped into a non-dimensional space by deploying the following transformations:

$$u = \frac{\partial \psi}{\partial y}, v = -\frac{\partial \psi}{\partial x}. \tag{13}$$

Using the following dimensionless variables: (see Watanabe [6]):

$$\xi = -\sqrt{\frac{1+m}{2}} \frac{V_w x}{\nu_f Re_x^{1/2}} \tag{14}$$

$$\eta = \sqrt{\frac{1+m}{2}} \frac{y}{x} Re_x^{1/2} \tag{15}$$

$$f(\xi, \eta) = \sqrt{\frac{1+m}{2}} \frac{\psi}{\nu_f Re_x^{1/2}} \tag{16}$$

$$\theta(\xi, \eta) = \frac{T - T_\infty}{T_w(x) - T_\infty} = \frac{T - T_\infty}{Ax^\lambda} \tag{17}$$

$$Re_x = \frac{U_e(x)x}{\nu_f} = \frac{Bx^{1+m}}{\nu_f} \tag{18}$$

It is pertinent to clarify that the current boundary layer problem is inherently non-similar due to the presence of uniform blowing/suction. Unlike a purely similarity solution, where the velocity and temperature profiles remain invariant along the wedge surface, the non-similar formulation explicitly accounts for the streamwise evolution of the boundary layer. The inclusion of the x-terms in the transformed equations (Eqs. (13)–(18)) allows the model to capture how the flow and thermal characteristics develop as the fluid moves downstream from the wedge apex.

In this transformed framework, ξ characterizes the uniform mass flux (blowing/suction) parameter and is a variable ($\xi \sim x^{1/2}$), η represents the pseudo-similarity coordinate, while $f(\xi, \eta)$ and $\theta(\xi, \eta)$ stand for the dimensionless stream function and temperature profiles, respectively. Re_x denotes the local Reynolds number based on the kinematic viscosity of the regular fluid (ν_f).

Drawing upon the spatial heat generation model proposed by Postelnicu et al. [14], the internal energy generation rate per unit volume (q''') is mathematically structured as:

$$q''' = A^* \frac{k_f[T_w(x) - T_\infty]Re_x}{x^2} e^{-\eta} \tag{19}$$

here, A^* acts as the amplitude coefficient for heat generation, where $A^* > 0$ denotes an active internal heat source. In Eq. (19), A^* defines the internal heat generation coefficient. The exponential term $e^{-\eta}$ mathematically represents the spatial decay of internal heating; it correctly assumes that heat generation is most intense near the solid boundary ($\eta = 0$) and exponentially decays to zero in the free stream ($\eta \to \infty$). Linking it to the pseudo-similarity variable η effectively models realistic boundary-layer heating profiles. Upon substituting the non-similarity variables and the heat source expression into the fundamental transport

equations, the original boundary layer system is rigorously reduced to the subsequent dimensionless formulations:

Dimensionless governing equations:

$$\begin{aligned}&\frac{\mu_{hnf}/\mu_f}{\rho_{hnf}/\rho_f}f''' + ff'' + \frac{2m}{1+m}\left[1-\left(f'\right)^2\right]\\&= \left(\frac{1-m}{1+m}\right)\xi\left(f'\frac{\partial f'}{\partial \xi} - f''\frac{\partial f'}{\partial \xi}\right).\end{aligned} \tag{20}$$

Dimensionless energy equation:

$$\begin{aligned}&\frac{1}{\mathrm{Pr}}\frac{1}{(\rho C_P)_{hnf}/(\rho C_P)_f}\left(\frac{k_{hnf}}{k_f}+\frac{4R}{3}\right)\theta'' + f\theta'\\&-\frac{2\lambda}{1+m}f'\theta + \frac{2}{1+m}\frac{A^*}{\mathrm{Pr}}\frac{1}{(\rho C_P)_{hnf}/(\rho C_P)_f}e^{-\eta}\\&= \left(\frac{1-m}{1+m}\right)\xi\left(f'\frac{\partial \theta}{\partial \xi} - \theta'\frac{\partial f}{\partial \xi}\right),\end{aligned} \tag{21}$$

Dimensionless boundary conditions:

$$\eta = 0 \,:\, f' = 0, f = \xi, \theta = 1, \tag{22}$$

$$\eta_\infty \to \infty \,:\, f' = 1, \theta = 0. \tag{23}$$

$$u = \frac{\nu_f Re_x}{x}f' = U_e(x)f', \tag{24}$$

$$v = -\sqrt{\frac{2}{1+m}}\frac{\nu_f Re_x^{1/2}}{x}\begin{bmatrix}\frac{1+m}{2}f + \frac{1-m}{2}\xi\frac{\partial f}{\partial \xi}\\ -\left(\frac{1-m}{2}\right)\eta f'\end{bmatrix}. \tag{25}$$

(Note: The primes denote differentiation with respect to η). Through integration of the continuity condition at the solid interface ($y = 0 \to \eta = 0$), the boundary condition evaluates to $f(\xi, 0) = \xi$. Consequently, suction corresponds to $V_w < 0$ ($\xi < 0$), whereas fluid injection (blowing) aligns with $V_w > 0$ ($\xi > 0$).

The relative dominance of thermal radiation is quantified by the radiation parameter R, formulated as:

$$R = \frac{4\sigma_o T_\infty^3}{k_f \chi}. \tag{26}$$

From a thermal engineering perspective, evaluating surface drag and heat dissipation is paramount. These physical quantities are characterized by the local skin-friction coefficient (C_f) and the local Nusselt number (Nu_x), defined conceptually as:

$$\begin{aligned}&C_f = \frac{\tau_w}{\rho_f[U_e(x)]^2/2},\\&Nu_x = \frac{h_f x}{k_f} = \frac{q_w x}{k_f[T_w(x)-T_\infty]}.\end{aligned} \tag{27}$$

Integrating the dimensionless transformations into the physical definitions yields the operational forms of the skin friction and heat transfer rates:

$$\tau_w = \mu_{hnf}\left.\frac{\partial u}{\partial y}\right|_{y=0},$$
$$q_w = q_{cond} + q_{rad} = -\left(k_{hnf} + \frac{16\sigma_o T_\infty^3}{3\chi}\right)\left(\frac{\partial T}{\partial y}\right)_{y=0} \tag{28}$$

Substituting Eqs. (7), (14)–(18), (26) and (28) into Eq. (27), we receive the local skin-friction coefficient in terms of $0.5C_f Re_x^{1/2}$ and the local Nusselt number in terms of $Nu_x/Re_x^{1/2}$:

$$0.5C_f Re_x^{1/2} = \sqrt{\frac{1+m}{2}}\frac{\mu_{hnf}}{\mu_f} f''(\xi, 0) \tag{29}$$

$$\frac{Nu_x}{Re_x^{1/2}} = \sqrt{\frac{1+m}{2}}\left(\frac{k_{hnf}}{k_f} + \frac{4R}{3}\right)\left[-\theta'(\xi, 0)\right] \tag{30}$$

This comprehensive framework encompasses several limiting scenarios. Specifically, neglecting thermal radiation, VWT, internal heating, and nanoparticle suspension ($R = \lambda = A^* = \varphi_1 = \varphi_2 = 0$) simplifies the system to the classical forced convection of a regular fluid (Watanabe [6]). Furthermore, adjusting the geometry to $m = 1$ or 0 perfectly models orthogonal stagnation or parallel flow without permeability. Lastly, nullifying all parameters except the nanoparticle volume fractions reduces the governing equations to the standard Blasius boundary layer problem for basic nanofluids, corroborating the foundational work of Ahmad et al. [38].

3 Numerical Procedure and Validation

The system of Eqs. (20)–(23) are solved by the Keller box method (KBM) of Cebeci & Bradshaw [44]. In the numerical implementation of the Keller-box scheme, the derivatives with respect to the streamwise coordinate ξ are discretized using a second-order central difference formula. This approach ensures that the non-similar nature of the governing equations is preserved, enabling a full-marching solution that tracks the boundary layer development along the ξ direction, rather than treating each location as an isolated similarity point. The Keller-box method, an implicit finite-difference scheme, was specifically chosen over standard Finite Element or explicit Finite Difference methods due to its unconditional stability, high accuracy for parabolic boundary-layer equations, and its robust capability to handle non-similar grid marching along the streamwise direction without losing numerical precision. The numerical computations are carried out on a personal computer. The variable grid parameter is 1.001 in the η direction with $\Delta\eta_1 = 0.0005$, $\eta_\infty = 16$, and $\Delta\xi = 0.01$ (uniform grid in the ξ direction). The iterative procedure is terminated when the errors in computing f''_w and θ'_w in the subsequent step are less than 10^{-5}.

In order to check the accuracy of our computer simulation model, we have compared our results with those of Watanabe [6], Kumari et al. [9], Ganapathirao et al. [17], Haq et al. [35], Yacob et al. [40], Ibrahim & Tulu [33], Amar & Kishan [34], Ahmad et al. [38] and Yacob et al. [39]. Table 2 illustrates the comparison of $-\theta'(0, 0)$ for various values of Pr with $m = 0.0909$, $\xi = 0$, $R = 0$, $\lambda = 0$, $A^* = 0$, $\varphi_1 = \varphi_2 = 0$. Table 3 shows the comparison of $f''(\xi, 0)$ and $-\theta'(\xi, 0)$ for various values of ξ with Pr = 0.73, $m = 0.0909$, $R = 0$, $\lambda = 0$, $A^* = 0$, $\varphi_1 = \varphi_2 = 0$. Tables 4 and 5 list the comparison of $f''(0, 0)$ and $-\theta'(0, 0)$ for various values of m with Pr = 0.73, $\xi = 0$, $R = 0$, $\lambda = 0$, $A^* = 0$, $\varphi_1 = \varphi_2 = 0$, respectively. Table 6 displays the comparison of $0.5C_f Re_x^{1/2}$ and $Nu_x/Re_x^{1/2}$ for various values of (a) Al_2O_3: φ_1 ($\varphi_2 = 0$) and (b) Cu: φ_2 ($\varphi_1 = 0$) with Pr = 6.2, $m = 0$, $\xi = 0$, $R = 0$, $\lambda = 0$, $A^* = 0$. Table 7 shows the comparison of $0.5C_f[2Re_x/(1+m)]^{1/2}$ and $Nu_x/[(1+m)Re_x/2]^{1/2}$ for various values of (a) m and Al_2O_3: φ_1 ($\varphi_2 = 0$) and (b) m and Cu: φ_2 ($\varphi_1 = 0$) with Pr = 6.2, $\xi = 0$, $R = 0$, $\lambda = 0$, $A^* = 0$. The comparisons in all the

above cases are found to be in good agreement, as shown in Tables 2–7. While the extensive validation presented in Tables 2–7 demonstrates excellent agreement with existing literature for various limiting cases (e.g., pure wedge flows, basic nanofluids, and isolated radiation effects), it is important to acknowledge a specific limitation. Direct validation of the fully coupled problem—simultaneously incorporating hybrid nanoparticles, thermal radiation, and exponential space-dependent heat generation—is currently precluded due to a lack of corresponding experimental or comprehensive numerical data in the open literature. Nevertheless, the robust convergence and high accuracy of the Keller-box method across these decoupled, fundamental scenarios provide substantial confidence in its capability and reliability when extending the mathematical framework to the present fully coupled multiphysics system.

Table 2: Comparison of $-\theta'(0,0)$ for various values of Pr with $m = 0.0909$, $\xi = 0$, $R = 0$, $\lambda = 0$, $A^* = 0$, $\varphi_1 = \varphi_2 = 0$.

Pr	$-\theta'(0,0)$	
	Watanabe [6]	Present Results
0.3	0.31967	0.31945
0.73	0.44730	0.44730
1	0.50198	0.50198
7	0.99634	0.99634
10	1.12618	1.12618
15	1.29360	1.29359

Table 3: Comparison of $f''(\xi,0)$ and $-\theta'(\xi,0)$ for various values of ξ with Pr $= 0.73$, $m = 0.0909$, $R = 0$, $\lambda = 0$, $A^* = 0$, $\varphi_1 = \varphi_2 = 0$.

ξ	$f''(\xi,0)$		$-\theta'(\xi,0)$	
	Watanabe [6]	Present Results	Watanabe [6]	Present Results
0.5	1.28787	1.28788	0.91425	0.91426
0.2	0.88709	0.88710	0.62013	0.62014
0	0.65498	0.65498	0.44370	0.44370
−0.2	0.45823	0.45823	0.29793	0.29794
−0.5	0.24317	0.24317	0.12899	0.12899

Table 4: Comparison of $f''(0,0)$ for various values of m with Pr $= 0.73$, $\xi = 0$, $R = 0$, $\lambda = 0$, $A^* = 0$, $\varphi_1 = \varphi_2 = 0$.

m	$f''(0,0)$					
	Watanabe [6]	Kumari et al. [9]	Ganapathirao et al. [17]	Haq et al. [35]	Yacob et al. [40]	Present Results
0	0.46960	0.46975	0.46972	0.46982	0.46960	0.46960
0.0141	0.50461	0.50472	0.50481	0.50495	—	0.50461
0.0435	0.56898	0.56904	0.56890	0.56944	—	0.56898
0.0909	0.65498	0.65501	0.65493	0.66433	0.65499	0.65498
0.1429	0.73200	0.73202	0.73196	0.73670	—	0.73200
0.2000	0.80213	0.80214	0.80215	0.80602	0.80213	0.80213
0.3333	0.92765	0.92766	0.92767	0.92905	0.92768	0.92765
0.5	—	—	—	—	1.03890	1.03890
1	—	—	—	1.23284	1.23259	1.23259

Table 5: Comparison of $-\theta'(0,0)$ for various values of m with Pr = 0.73, $\xi = 0$, $R = 0$, $\lambda = 0$, $A^* = 0$, $\varphi_1 = \varphi_2 = 0$.

m	$-\theta'(0,0)$				
	Watanabe [6]	**Ibrahim & Tulu [33]**	**Amar & Kishan [34]**	**Haq et al. [35]**	**Present Results**
0	0.42015	0.42016	0.4212	0.42151	0.42015
0.0141	0.42578	0.42578	0.4268	0.42876	0.42578
0.0435	0.43548	0.43548	0.4363	0.43641	0.43548
0.0909	0.44730	0.44730	0.4713	0.47211	0.44730
0.1429	0.45693	0.45694	0.4789	0.47923	0.45693
0.2000	0.46503	0.46503	0.4855	0.48645	0.46503
0.3333	0.47814	0.47814	0.4966	0.49733	0.47814
0.5	—	—	—	—	0.48848
1	—	—	0.5196	0.52663	0.50418

Table 6: Comparison of $0.5C_f Re_x^{1/2}$ and $Nu_x/Re_x^{1/2}$ for various values of (a) Al_2O_3: φ_1 ($\varphi_2 = 0$) and (b) Cu: φ_2 ($\varphi_1 = 0$) with Pr = 6.2, $m = 0$, $\xi = 0$, $R = 0$, $\lambda = 0$, $A^* = 0$.

(a) Al_2O_3 : φ_1 ($\varphi_2 = 0$)	$0.5C_f Re_x^{1/2}$		$Nu_x/Re_x^{1/2}$	
	Ahmad et al. [38]	**Present Results**	**Ahmad et al. [38]**	**Present Results**
0.0	0.3321	0.3321	0.6201	0.6201
0.01	0.3412	0.3412	—	0.6318
0.02	0.3506	0.3506	—	0.6435
0.1	0.4316	0.4316	—	0.7370
0.2	0.5545	0.5545	—	0.8550
(b) Cu : φ_2 ($\varphi_1 = 0$)	$0.5C_f Re_x^{1/2}$		$Nu_x/Re_x^{1/2}$	
	Ahmad et al. [38]	**Present Results**	**Ahmad et al. [38]**	**Present Results**
0.0	0.3321	0.3321	0.6201	0.6201
0.01	0.3494	0.3494	—	0.6374
0.02	0.3667	0.3667	—	0.6544
0.1	0.5076	0.5076	—	0.7850
0.2	0.7066	0.7066	—	0.9435

Table 7: Comparison of $0.5C_f[2Re_x/(1+m)]^{1/2}$ and $Nu_x/[(1+m)Re_x/2]^{1/2}$ for various values of (a) m and Al_2O_3: φ_1 ($\varphi_2 = 0$) and (b) m and Cu: φ_2 ($\varphi_1 = 0$) with Pr = 6.2, $\xi = 0$, $R = 0$, $\lambda = 0$, $A^* = 0$.

(a) m	Al_2O_3 : φ_1 ($\varphi_2 = 0$)	$0.5C_f[2Re_x/(1+m)]^{1/2}$		$Nu_x/[(1+m)Re_x/2]^{1/2}$	
		Yacob et al. [39]	**Present Results**	**Yacob et al. [39]**	**Present Results**
0	0.1	0.6103	0.6104	1.0423	1.0423
	0.2	0.7842	0.7842	1.2092	1.2092
0.5	0.1	1.3502	1.3503	1.2744	1.2743
	0.2	1.7348	1.7349	1.4718	1.4718
1	0.1	1.6019	1.6021	1.3305	1.3305
	0.2	2.0584	2.0583	1.5352	1.5352
(b) m	Cu : φ_2 ($\varphi_1 = 0$)	$0.5C_f[2Re_x/(1+m)]^{1/2}$		$Nu_x/[(1+m)Re_x/2]^{1/2}$	
		Yacob et al. [39]	**Present Results**	**Yacob et al. [39]**	**Present Results**
0	0.1	0.7179	0.7179	1.1100	1.1101
	0.2	0.9992	0.9992	1.3342	1.3342
0.5	0.1	1.5881	1.5882	1.3472	1.3473
	0.2	2.2105	2.2106	1.6048	1.6049
1	0.1	1.8843	1.8843	1.4043	1.4043
	0.2	2.6226	2.6227	1.6692	1.6693

4 Results and Discussion

A comprehensive parametric analysis was conducted to evaluate the hydrothermal behavior of the boundary layer, with numerical outcomes presented across specific variable ranges: the wedge angle parameter (m) spans from 0 (Blasius flow) to 1 (Hiemenz flow), the surface mass flux parameter (ξ) varies between 0.2 (suction) and −0.2 (blowing), and the thermal radiation parameter (R) is adjusted from 0 to 2. Additionally, the evaluations incorporate a variable wall temperature exponent (λ) and an internal heat generation coefficient (A^*) ranging from 0 to 2, alongside solid volume fractions for Al_2O_3 (φ_1) up to 0.1 and Cu (φ_2) up to 0.05. To illustrate the non-similar behavior, the dimensionless velocity and temperature profiles presented in subsequent figures are extracted at specific streamwise locations. This distinction is crucial, as it highlights that the boundary layer structure is not fixed but is a function of the distance along the wedge, influenced by the cumulative effects of surface mass transfer.

Impact of Wedge Angle Parameter (m)

Visualizations of the dimensionless velocity and temperature distributions under varying wedge angles are depicted in Figs. 2 and 3. Expanding the wedge angle parameter visibly accelerates the fluid, thereby augmenting the wall velocity gradient while compressing the momentum boundary layer. Conversely, thermal characteristics exhibit an inverse relationship; both the temperature profiles and the thermal boundary layer thickness contract as m rises, which consequently steepens the temperature gradient at the wall. These graphical trends are quantitatively supported by Table 8, indicating a simultaneous surge in both the local skin-friction coefficient ($0.5C_fRe_x^{1/2}$) and the local Nusselt number ($Nu_x/Re_x^{1/2}$) when m is increased. This overall enhancement directly stems from the amplified velocity and temperature gradients near the surface.

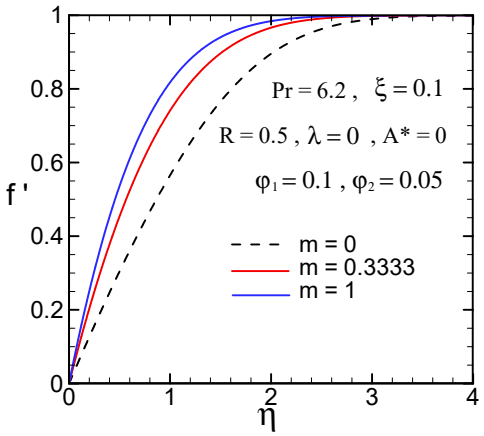

Figure 2: The dimensionless velocity profiles (f') for varying wedge angle parameters (m) with fixed conditions: Pr = 6.2, $\xi = 0.1$, $R = 0.5$, $\lambda = 0$, $A^* = 0$, $\varphi_1 = 0.1$, $\varphi_2 = 0.05$.

Table 8: $0.5C_fRe_x^{1/2}$ and $Nu_x/Re_x^{1/2}$ for five values of m with Pr = 6.2, $\xi = 0.1$, $R = 0.5$, $\lambda = 0$, $A^* = 0$, $\varphi_1 = 0.1$, $\varphi_2 = 0.05$.

m	$0.5C_fRe_x^{1/2}$	$Nu_x/Re_x^{1/2}$
0	0.6759	1.5680
0.1429	1.0074	1.7153
0.3333	1.3169	1.8612
0.5	1.5335	1.9697
1	2.0421	2.2443

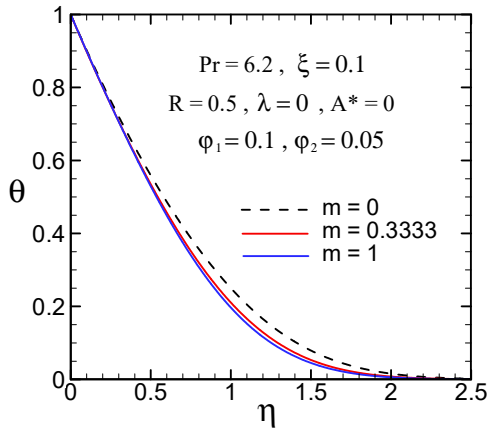

Figure 3: The dimensionless temperature profiles (θ) for varying wedge angle parameters (m) with fixed conditions: Pr = 6.2, $\xi = 0.1$, $R = 0.5$, $\lambda = 0$, $A^* = 0$, $\varphi_1 = 0.1$, $\varphi_2 = 0.05$.

Influence of Surface Mass Flux (ξ)

The profound influence of surface mass flux is captured in Figs. 4 and 5, alongside Table 9. Applying suction ($\xi > 0$) facilitates fluid removal at the boundary, effectively thinning both the momentum and thermal boundary layers. This compression leads to steeper velocity and temperature gradients at the wall, translating into elevated skin friction and a higher convective heat transfer rate. In contrast, fluid injection or blowing ($\xi < 0$) thickens these boundary layers, acting as a buffer that diminishes both wall shear stress and thermal dissipation. Notably, comparing Figs. 3 and 5 reveals that the thermal profiles are significantly more responsive to changes in the mass flux parameter than to geometric variations represented by m. Beyond a purely descriptive analysis, these mass flux effects have significant implications for active boundary-layer control strategies in thermal engineering. Continuous suction ($\xi > 0$) can be strategically employed to delay boundary layer separation and physically draw hotter near-wall fluid away, thereby maintaining a dynamically thin boundary layer that maximizes convective cooling efficiency. Conversely, blowing or fluid injection ($\xi < 0$) acts as a form of transpiration cooling; by continuously injecting fluid from the porous surface, it creates a thickened thermal buffer zone. While this reduces the local Nusselt number, it is an intentional and highly effective strategy utilized in aerospace applications to shield solid surfaces from extreme external heat fluxes.

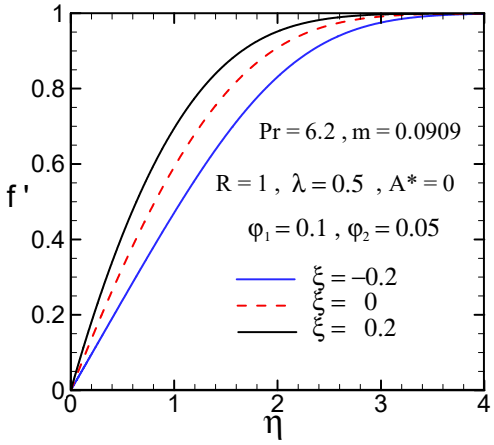

Figure 4: Influence of surface mass flux parameter (ξ) on dimensionless velocity distributions f' with constant Pr = 6.2, $m = 0.0909$, $R = 1$, $\lambda = 0.5$, $A^* = 0$, $\varphi_1 = 0.1$, $\varphi_2 = 0.05$.

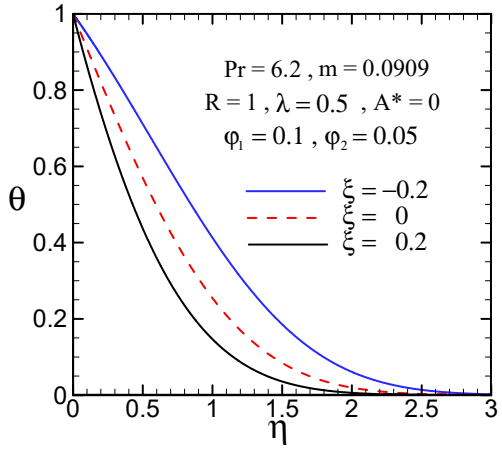

Figure 5: Influence of surface mass flux parameter (ξ) on dimensionless temperature distributions θ with constant Pr = 6.2, $m = 0.0909$, $R = 1$, $\lambda = 0.5$, $A^* = 0$, $\varphi_1 = 0.1$, $\varphi_2 = 0.05$.

Table 9: $0.5C_f Re_x^{1/2}$ and $Nu_x/Re_x^{1/2}$ for five values of ξ with Pr = 6.2, $m = 0.0909$, $R = 1$, $\lambda = 0.5$, $A^* = 0$, $\varphi_1 = 0.1$, $\varphi_2 = 0.05$.

ξ		$0.5C_f Re_x^{1/2}$	$Nu_x/Re_x^{1/2}$
−0.2	(blowing)	0.5202	1.0714
−0.1		0.6351	1.4623
0		0.7629	1.9167
0.1		0.9023	2.4283
0.2	(suction)	1.0524	2.9899

Effects of Thermal Radiation (R)

Fig. 6 and Table 10 elucidate the role of thermal radiation. Because the momentum balance remains independent of radiation in this formulation, velocity profiles are completely unaffected by changes in R. However, intensified radiative heat transfer ($R > 0$) injects additional thermal energy into the fluid, causing the thermal boundary layer to expand and overall fluid temperatures to rise.

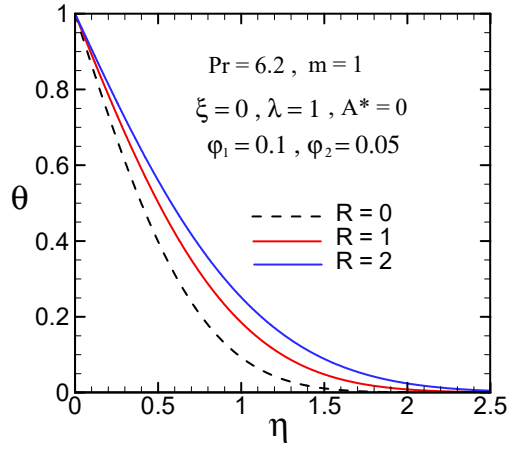

Figure 6: Dimensionless temperature profiles θ for varying thermal radiation parameter (R) at fixed Pr = 6.2, $m = 1$, $\xi = 0$, $\lambda = 1$, $A^* = 0$, $\varphi_1 = 0.1$, $\varphi_2 = 0.05$.

Table 10: $0.5C_fRe_x^{1/2}$ and $Nu_x/Re_x^{1/2}$ for five values of R with Pr = 6.2, $m = 1$, $\xi = 0$, $\lambda = 1$, $A^* = 0$, $\varphi_1 = 0.1$, $\varphi_2 = 0.05$.

R	$0.5C_fRe_x^{1/2}$	$Nu_x/Re_x^{1/2}$
0	1.9349	2.0756
0.5	1.9349	2.6176
1	1.9349	3.0993
1.5	1.9349	3.5389
2	1.9349	3.9470

Despite the broader temperature distribution resulting in a slightly less steep dimensionless wall temperature gradient (θ), an upward trend in the overall local Nusselt number ($Nu_x/Re_x^{1/2}$) is prominently observed. It is crucial to interpret this result with care: this enhancement does not imply a stronger purely convective heat transfer. Rather, as explicitly defined in Eq. (30), the total effective Nusselt number incorporates the radiation parameter directly via the term $\left(k_{hnf}/k_f + 4R/3\right)$. Therefore, the significant increase in the direct radiative energy transport successfully compensates for and overcomes the diminished conductive/convective thermal gradient, leading to an augmented overall surface heat transfer rate rather than a purely convective enhancement.

Role of Variable Wall Temperature (λ)

Fig. 7 and Table 11 examine the ramifications of the wall temperature exponent. Elevating λ effectively narrows the thermal boundary layer, which fundamentally drives up the temperature gradient at the solid-fluid interface. Consequently, while the skin friction remains isolated from this specific thermal boundary condition ($0.5C_fRe_x^{1/2}$ remains constant at 1.3169), the local Nusselt number experiences a consistent enhancement as λ grows.

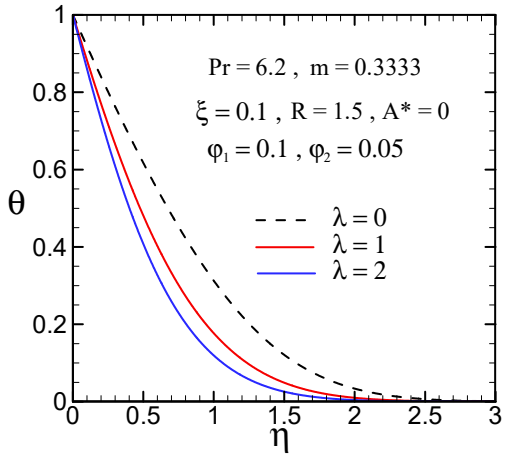

Figure 7: Impact of wall temperature exponent (λ) on dimensionless temperature profiles θ with constant Pr = 6.2, $m = 0.3333$, $\xi = 0.1$, $R = 1.5$, $A^* = 0$, $\varphi_1 = 0.1$, $\varphi_2 = 0.05$.

Table 11: $0.5C_fRe_x^{1/2}$ and $Nu_x/Re_x^{1/2}$ for five values of λ with Pr = 6.2, $m = 0.3333$, $\xi = 0.1$, $R = 1.5$, $A^* = 0$, $\varphi_1 = 0.1$, $\varphi_2 = 0.05$.

λ	$0.5C_fRe_x^{1/2}$	$Nu_x/Re_x^{1/2}$
0	1.3169	2.3637
0.5	1.3169	2.9889
1	1.3169	3.4344
1.5	1.3169	3.7880
2	1.3169	4.0852

Internal Heat Generation (A^*) and the "Temperature Overshoot" Phenomenon

The critical effects of the space-dependent internal heat generation coefficient are portrayed in Fig. 8 and Table 12. A rise in A^* adds excess energy into the system, broadening the thermal boundary layer and systematically deteriorating the local Nusselt number. A pivotal phenomenon emerges at elevated heat generation levels (e.g., A^* = 1.5 or 2): a "temperature overshoot". Under these conditions, the volumetric heat produced within the boundary layer outpaces the convective cooling capacity, causing the fluid's peak temperature to exceed the surface temperature itself. This anomaly triggers a gradient inversion at the wall, driving thermal energy backward from the adjacent fluid into the wedge—a reversal mathematically reflected by negative Nusselt numbers. From a thermodynamic and engineering perspective, a negative Nusselt number signifies a fundamental shift from a wall-cooling regime to a wall-heating regime. Rather than the fluid acting as a heat sink to cool the surface, the "temperature overshoot" causes the adjacent fluid to become hotter than the wedge itself. Consequently, thermal energy is actively transferred from the fluid into the solid boundary. In practical thermal management applications, this indicates a complete failure of the cooling mechanism, as the intended coolant transforms into an additional heat source that could induce thermal damage to the structure. Understanding this overshoot is paramount for identifying thermal limits in extreme engineering scenarios. As A^* surpasses a critical threshold (e.g., $A^* > 1.5$), the internal volumetric heat generation overwhelms. Mathematically, this results in a negative Nusselt number. Physically, this means the wall is no longer cooling the fluid; instead, the fluid is actively heating the wall (wall heating). In an engineering context, crossing this threshold signifies a catastrophic failure of the cooling system, making these parameters vital for setting thermal safety limits.

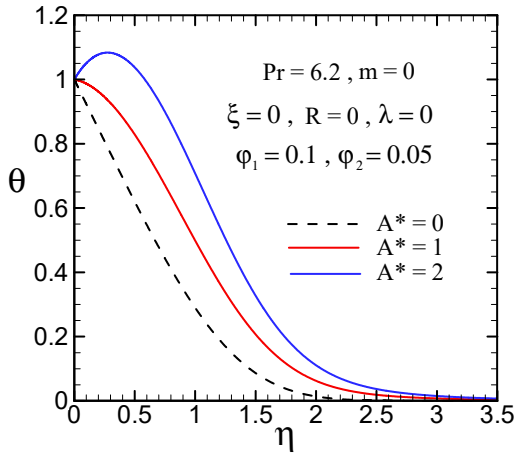

Figure 8: Dimensionless temperature profiles θ illustrating temperature overshoot for varying heat generation coefficient (A^*) at fixed Pr = 6.2, $m = 0$, $\xi = 0$, $R = 0$, $\lambda = 0$, $\varphi_1 = 0.1$, $\varphi_2 = 0.05$.

Table 12: $0.5C_f Re_x^{1/2}$ and $Nu_x/Re_x^{1/2}$ for five values of A^* with Pr = 6.2, $m = 0$, $\xi = 0$, $R = 0$, $\lambda = 0$, $\varphi_1 = 0.1$, $\varphi_2 = 0.05$.

A^*	$0.5C_f Re_x^{1/2}$	$Nu_x/Re_x^{1/2}$
0	0.5237	0.8267
0.5	0.5237	0.4491
1	0.5237	0.0716
1.5	0.5237	−0.3060
2	0.5237	−0.6835

Performance of Hybrid Nanoparticles (φ_1, φ_2)

Finally, the synergistic application of hybrid nanoparticles is evaluated in Figs. 9 and 10 and Tables 13 and 14. Introducing higher volume fractions of Al_2O_3 (φ_1) and Cu (φ_2) markedly accelerates the flow velocity adjacent to the wall and expands the thermal boundary layer due to the enhanced effective thermal conductivity of the formulated mixture. Although a thicker thermal boundary layer typically flattens the dimensionless wall temperature gradient, the superior inherent conductivity of the hybrid nanofluid overwhelmingly compensates for this geometric drop. Consequently, both the local skin friction and the overall heat transfer efficiency (Nusselt number) undergo significant improvements compared to the conventional base fluid, confirming the hydrothermal superiority of the hybrid configuration. However, the pronounced hydrothermal benefits associated with higher nanoparticle volume fractions must be critically evaluated against practical engineering penalties. Increasing the solid loading intrinsically elevates the mixture's effective dynamic viscosity, which in turn demands a substantially higher pumping power to maintain the desired flow rate, potentially offsetting the energetic gains from enhanced heat transfer. Furthermore, at elevated concentrations, the risk of nanoparticle agglomeration and sedimentation significantly increases. Such physical instabilities could degrade the performance of the hybrid nanofluid over time and cause the actual heat transfer enhancement to deviate from the idealized predictions of the present homogeneous single-phase model.

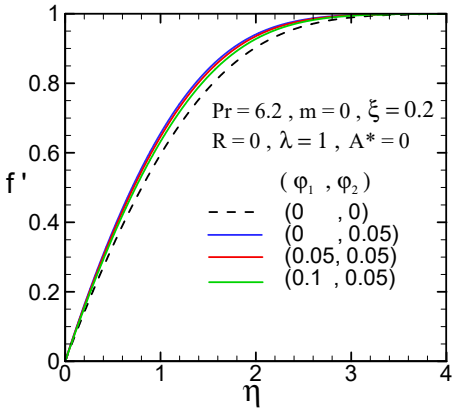

Figure 9: Effects of nanoparticle volume fractions (φ_1, φ_2) on dimensionless velocity profiles f' for $Al_2O_3 - Cu$/water hybrid nanofluid at Pr = 6.2, $m = 0$, $\xi = 0.2$, $R = 0$, $\lambda = 1$, $A^* = 0$.

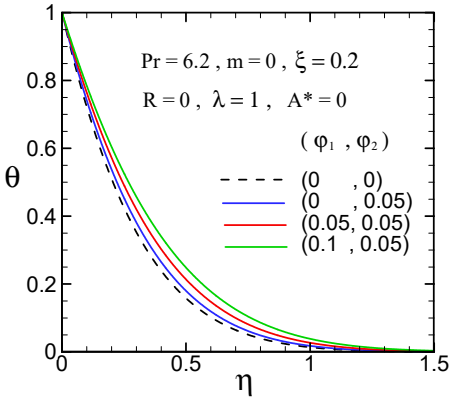

Figure 10: Effects of nanoparticle volume fractions (φ_1, φ_2) on dimensionless temperature profiles θ for $Al_2O_3 - Cu$/water hybrid nanofluid at Pr = 6.2, $m = 0$, $\xi = 0.2$, $R = 0$, $\lambda = 1$, $A^* = 0$.

Table 13: μ_{hnf}/μ_f, $f''(\xi,0)$, and $0.5C_fRe_x^{1/2}$ for four values of Al_2O_3: φ_1 and Cu: φ_2 with Pr = 6.2, $m = 0$, $\xi = 0.2$, $R = 0$, $\lambda = 1$, $A^* = 0$.

Al_2O_3: φ_1	Cu: φ_2	μ_{hnf}/μ_f	$f''(\xi,0)$	$0.5C_fRe_x^{1/2}$
0.0	0.0	1	0.7348	0.5196
0.0	0.05	1.1368	0.8493	0.6828
0.05	0.05	1.2924	0.8305	0.7589
0.1	0.05	1.4794	0.8034	0.8404

Table 14: k_{hnf}/k_f, $-\theta'(\xi,0)$, and $Nu_x/Re_x^{1/2}$ for four values of Al_2O_3: φ_1 and Cu: φ_2 with Pr = 6.2, $m = 0$, $\xi = 0.2$, $R = 0$, $\lambda = 1$, $A^* = 0$.

Al_2O_3: φ_1	Cu: φ_2	k_{hnf}/k_f	$-\theta'(\xi,0)$	$Nu_x/Re_x^{1/2}$
0.0	0.0	1	3.1582	2.2332
0.0	0.05	1.1571	2.8891	2.3639
0.05	0.05	1.3311	2.5959	2.4434
0.1	0.05	1.5235	2.3434	2.5246

5 Conclusions

This study computationally investigates the forced convective boundary layer flow of an Al_2O_3-Cu/water hybrid nanofluid over a non-isothermal wedge. By incorporating exponential space-dependent heat generation (ESDHG), thermal radiation, and uniform surface mass flux into a non-similar formulation, the governing equations were solved utilizing the Keller-box scheme. The principal findings are summarized as follows:

- **Geometric Influence:** Increasing the wedge angle parameter (m) accelerates the external flow, which effectively thins the momentum boundary layer. This aerodynamic compression leads to a simultaneous increase in both the local skin-friction coefficient and the convective heat transfer rate.
- **Hybrid Nanoparticle Trade-Offs:** Higher volume fractions of hybrid nanoparticles (φ_1, φ_2) notably enhance the effective thermal conductivity of the fluid, thereby improving the local Nusselt number. However, this thermal benefit is accompanied by elevated dynamic viscosity and skin friction, necessitating a careful engineering trade-off between cooling efficiency and the required pumping power.
- **Thermal Radiation Effects:** The application of the Rosseland diffusion approximation reveals that thermal radiation (R) thickens the thermal boundary layer and elevates the overall fluid temperature. Although this flattens the local temperature gradient at the wall, the augmented direct radiative energy transport ultimately results in a higher total effective Nusselt number.
- **Boundary Layer Control:** Surface suction ($\xi > 0$) successfully minimizes the thermal boundary layer thickness, enhancing local cooling performance. Conversely, fluid injection or blowing ($\xi < 0$) thickens the thermal buffer zone, which decreases the local heat transfer coefficient but can serve as an effective transpiration cooling strategy to shield the surface from extreme external temperatures.
- **Heat-Flux Reversal:** Under conditions of strong internal heat generation (A^*), a critical "temperature overshoot" occurs, shifting the system into a negative Nusselt number regime. This mathematically denotes a physical transition from wall cooling to wall heating, where the fluid transfers energy back into the solid structure. Identifying this threshold is vital for preventing thermal runaway in practical thermal management systems.

Through this comprehensive parametric evaluation, it is observed that the surface mass flux parameter and the heat generation coefficient exert the most dominant sensitivity on the local Nusselt number,

effectively overriding the geometric influences of the wedge angle. While the present study offers foundational insights within the laminar regime, several avenues remain for future exploration. Subsequent investigations should consider adopting multiphase frameworks to better capture micro-scale solid-fluid interactions and employing advanced radiative models to address optically thin conditions in extreme thermal environments. Furthermore, evaluating the effects of massive transpiration (suction/blowing) under higher Reynolds number turbulent conditions is essential, as turbulent eddy viscosity may significantly alter the transpiration cooling efficiency.

Acknowledgement: The author expresses his appreciation to Professor K. A. Yih for the guidance on numerical computation and reading of the manuscript.

Funding Statement: The author received no specific funding for this study.

Availability of Data and Materials: Data sharing is not applicable to this article as no new data were created or analyzed in this study.

Ethics Approval: This research did not involve human participants or animal subjects; thus, ethical approval was not required.

Conflicts of Interest: The author declares no conflicts of interest.

Nomenclature

A^*	internal heat generation coefficient
A	constant
B	constant
C_P	specific heat at constant pressure
f	dimensionless stream function
k	equivalent thermal conductivity
m	wedge angle parameter
Nu_x	local Nusselt number
q	heat flux
q_{rad}	radiation heat flux
q'''	internal heat generation rate per unit volume
R	thermal radiation parameter
Re_x	local Reynolds number
T	temperature
u	Darcian velocity component in the x-direction
U_e	velocity of the external free stream
v	Darcian velocity component in the y-direction
x	streamwise coordinate
y	transverse coordinate

Greek symbols

τ_w	wall shear stress
ξ	blowing/suction parameter
η	pseudo-similarity variable
θ	dimensionless temperature
λ	variable wall temperature exponent
μ	absolute viscosity of fluid
ρ	density of fluid
σ_0	Stefan-Boltzmann constant
ψ	stream function
χ	Rosseland mean absorption coefficient
γ	wedge with a half angle

Subscripts

f	fluid
hnf	hybrid nanofluid
nf	nanofluid
w	condition at the wall
∞	condition at infinity

References

1. Schlichting H, Gersten K. Boundary-layer theory. Berlin/Heidelberg, Germany: Springer; 2000. [CrossRef].
2. Falkneb VM, Skan SW. LXXXV. Solutions of the boundary-layer equations. Lond Edinb Dublin Philos Mag J Sci. 1931;12(80):865–96. [CrossRef].
3. Koh JCY, Hartnett JP. Skin friction and heat transfer for incompressible laminar flow over porous wedges with suction and variable wall temperature. Int J Heat Mass Transf. 1961;2(3):185–98. [CrossRef].
4. Ye-Mon C. Heat transfer of a laminar flow passing a wedge at small Prandtl number: a new approach. Int J Heat Mass Transf. 1985;28(8):1517–23. [CrossRef].

5. Lin HT, Lin LK. Similarity solutions for laminar forced convection heat transfer from wedges to fluids of any Prandtl number. Int J Heat Mass Transf. 1987;30(6):1111–8. [CrossRef].
6. Watanabe T. Thermal boundary layers over a wedge with uniform suction or injection in forced flow. Acta Mech. 1990;83(3):119–26. [CrossRef].
7. Yih KA. Uniform suction/blowing effect on forced convection about a wedge: uniform heat flux. Int Commun Heat Mass. 1998;128:173–81. [CrossRef].
8. Hossain MA, Munir MS, Rees DAS. Flow of viscous incompressible fluid with temperature dependent viscosity and thermal conductivity past a permeable wedge with uniform surface heat flux. Int J Therm Sci. 2000;39(6):635–44. [CrossRef].
9. Kumari M, Takhar HS, Nath G. Mixed convection flow over a vertical wedge embedded in a highly porous medium. Heat Mass Transf. 2001;37(2):139–46. [CrossRef].
10. Takhar HS, Chamkha AJ, Nath G. Unsteady mixed convection flow from a rotating vertical cone with a magnetic field. Heat Mass Transf. 2003;39(4):297–304. [CrossRef].
11. Ishak A, Nazar R, Pop I. Falkner-Skan equation for flow past a moving wedge with suction or injection. J Appl Math Comput. 2007;25(1):67–83. [CrossRef].
12. Hai T, Mansir IB, Alshuraiaan B, M Abed A, Elhosiny Ali H, Dahari M, et al. Numerical investigation on the performance of a solar air heater using inclined impinging jets on absorber plate with parallel and crossing orientation of nozzles. Case Stud Therm Eng. 2023;45:102913. [CrossRef].
13. Hussain M, Ali Khan M, Waqas H, Shekar S. Thermal insights into magnetized ternary nanofluid flow: a novel paradigm integrating graph-neural network and Keller-box approach. Eng Appl Comput Fluid Mech. 2026;20(1):2597952. [CrossRef].
14. Postelnicu A, Groşan T, Pop I. The effect of variable viscosity on forced convection flow past a horizontal flat plate in a porous medium with internal heat generation. Mech Res Commun. 2001;28(3):331–7. [CrossRef].
15. Magyari E, Chamkha AJ. Combined effect of heat generation or absorption and first-order chemical reaction on micropolar fluid flows over a uniformly stretched permeable surface: the full analytical solution. Int J Therm Sci. 2010;49(9):1821–8. [CrossRef].
16. Sharma PR, Singh G. Effects of variable thermal conductivity and heat source/sink on MHD flow near a stagnation point on a linearly stretching sheet. J Appl Fluid Mech. 2009;2(1):13–21. [CrossRef].
17. Ganapathirao M, Ravindran R, Momoniat E. Effects of chemical reaction, heat and mass transfer on an unsteady mixed convection boundary layer flow over a wedge with heat generation/absorption in the presence of suction or injection. Heat Mass Transf. 2015;51(2):289–300. [CrossRef].
18. Ragupathi P, Saranya S, Mittal HVR, Al-Mdallal QM. Computational study on three-dimensional convective casson nanofluid flow past a stretching sheet with Arrhenius activation energy and exponential heat source effects. Complexity. 2021;2021:5058751. [CrossRef].
19. Sparrow EM, Cess RD. Radiation heat transfer. Belmont, CA, USA: Brooks/Cole Publishing Company; 1962.
20. Salawu SO, Ogunseye HA, Yusuf TA, Lebelo RS, Mustapha RA. Entropy generation in a magnetohydrodynamic hybrid nanofluid flow over a nonlinear permeable surface with velocity slip effect. Wseas Trans Fluid Mech. 2023;18:34–48. [CrossRef].
21. Siddique I, Khan Y, Nadeem M, Awrejcewicz J, Bilal M. Significance of heat transfer for second-grade fuzzy hybrid nanofluid flow over a stretching/shrinking Riga wedge. AIMS Math. 2023;8(1):295–316. [CrossRef].
22. Chakraborty A, Saadeh R, Qazza A, Zomot N, Janapatla P, Khan U, et al. On the thermal performance of radiative stagnation-point hybrid nanofluid flow across a wedge with heat source/sink effects and sensitivity analysis. Front Mater. 2024;11:1391377. [CrossRef].
23. Nath RS, Deka RK. A numerical study on the MHD ternary hybrid nanofluid (Cu-Al_2O_3-TiO_2/H_2O) in presence of thermal stratification and radiation across a vertically stretching cylinder in a porous medium. East Eur J Phys. 2024:232–42. [CrossRef].
24. Sakkaravarthi K, Reddy PBA, Sakthi I. Entropy optimization in Casson tetra-hybrid nanofluid flow over a rotating disk with nonlinear thermal radiation: a Levenberg–Marquardt neural network approach. J Comput Des Eng. 2024;11(5):333–54. [CrossRef].

25. Alharbi AF, Mohammad F, Usman M, Khan N, Abushiba W. Thermophysical analysis of time-dependent magnetized Casson hybrid nanofluid flow (Cu + GO/Kerosene Oil) using Darcy-Forchheimer and thermal radiative models for industrial cooling applications. Sci Rep. 2025;15(1):3398. [CrossRef].
26. Choi SUS. Enhancing thermal conductivity of fluids with nanoparticles. ASME Publ Fed. 1995;231:99–105. [CrossRef].
27. Kasaeian A, Daneshazarian R, Mahian O, Kolsi L, Chamkha AJ, Wongwises S, et al. Nanofluid flow and heat transfer in porous media: a review of the latest developments. Int J Heat Mass Transf. 2017;107:778–91. [CrossRef].
28. Kshirsagar DP, Venkatesh MA. A review on hybrid nanofluids for engineering applications. Mater Today Proc. 2021;44:744–55. [CrossRef].
29. Minkowycz WJ, Sparrow EM, Abraham JP. Nanoparticle heat transfer and fluid flow. Boca Raton, FL, USA: CRC Press; 2013.
30. Ali N. Hybrid nanofluids for convection heat transfer. Cambridge, MA, USA: Academic Press; 2020.
31. Chamkha AJ, Rashad AM. MHD forced convection flow of a nanofluid adjacent to a non-isothermal wedge. Comput Thermal Scien. 2014;6(1):27–39. [CrossRef].
32. Zaib A, Rashidi MM, Chamkha AJ. Flow of nanofluid containing gyrotactic microorganisms over static wedge in darcy-brinkman porous medium with convective boundary condition. J Por Media. 2018;21(10):911–28. [CrossRef].
33. Ibrahim W, Tulu A. Magnetohydrodynamic (MHD) boundary layer flow past a wedge with heat transfer and viscous effects of nanofluid embedded in porous media. Math Probl Eng. 2019;2019:4507852. [CrossRef].
34. Amar N, Kishan N. The influence of radiation on MHD boundary layer flow past a nano fluid wedge embedded in porous media. Partial Differ Equ Appl Math. 2021;4:100082. [CrossRef].
35. Haq EU, Khan SU, Abbas T, Smida K, Hassan QMU, Ahmad B, et al. Numerical aspects of thermo migrated radiative nanofluid flow towards a moving wedge with combined magnetic force and porous medium. Scientific Reports. 2022;12:10120. [CrossRef].
36. Tiwari RK, Das MK. Heat transfer augmentation in a two-sided lid-driven differentially heated square cavity utilizing nanofluids. Int J Heat Mass Transf. 2007;50(9–10):2002–18. [CrossRef].
37. Oztop HF, Abu-Nada E. Numerical study of natural convection in partially heated rectangular enclosures filled with nanofluids. Int J Heat Fluid Flow. 2008;29(5):1326–36. [CrossRef].
38. Ahmad S, Arifin NM, Pop I. Forced convection boundary layer flow of a nanofluid past a convex/concave stretching sheet. Chin Phys Lett. 2011;28(11):114702. [CrossRef].
39. Yacob NA, Ishak A, Pop I. Falkner–Skan problem for a static or moving wedge in nanofluids. Int J Therm Sci. 2011;50(2):133–9. [CrossRef].
40. Yacob NA, Ishak A, Nazar R, Pop I. Falkner–Skan problem for a static and moving wedge with prescribed surface heat flux in a nanofluid. Int Commun Heat Mass Transf. 2011;38(2):149–53. [CrossRef].
41. Murad NM, Rawi NA, Shafie S, Lim YJ, Mahat R. Unsteady falkner-skan flow of hybrid nanofluid over a nonlinear moving wedge. Mal J Fund Appl Sci. 2022;18(1):116–23. [CrossRef].
42. Wahid NS, Md Arifin N, Khashi'ie NS, Pop I, Bachok N, Hafidzuddin MEH. MHD mixed convection flow of a hybrid nanofluid past a permeable vertical flat plate with thermal radiation effect. Alex Eng J. 2022;61(4):3323–33. [CrossRef].
43. Gangadhar K, Mary Victoria E, Chamkha AJ. Hydrothermal features in the swirling flow of radiated graphene–Fe_3O_4 hybrid nanofluids through a rotating cylinder with exponential space-dependent heat generation. Waves Random Complex Media. 2025;35(5):8801–24. [CrossRef].
44. Cebeci T, Bradshaw P. Physical and computational aspects of convective heat transfer. New York, NY, USA: Springer; 1988. [CrossRef].
45. Alwan AA, Alomari MA, Hassan AM, Salho AK, Sadeq AM, Alqurashi F, et al. Synergistic heat transfer enhancement in triangular enclosures: hybrid nanofluid-porous wavy fin systems under magnetohydrodynamic and radiation effects. Energy Sci Eng. 2025;13(12):5924–48. [CrossRef].